Influence of Beam Broadening on the Accuracy of Radar Polarimetric Rainfall Estimation

EUGENIO GORGUCCI AND LUCA BALDINI

Istituto di Scienze dell'Atmosfera e del Clima, Consiglio Nazionale delle Ricerche, Area di Ricerca Roma-Tor Vergata, Rome, Italy

(Manuscript received 29 April 2014, in final form 20 January 2015)

ABSTRACT

The quantitative estimation of rain rates using meteorological radar has been a major theme in radar meteorology and radar hydrology. The increase of interest in polarimetric radar is in part because polarization diversity can reduce the effect on radar precipitation estimates caused by raindrop size variability, which has allowed progress on radar rainfall estimation and on hydrometeorological applications. From an operational point of view, the promises regarding the improvement of radar rainfall accuracy have not yet been completely proven. The main reason behind these limits is the geometry of radar measurements combined with the variability of the spatial structure of the precipitation systems. To overcome these difficulties, a methodology has been developed to transform the estimated drop size distribution (DSD) provided by a vertically pointing micro rain radar to a profile given by a ground-based polarimetric radar. As a result, the rainfall rate at the ground is fixed at all ranges, whereas the broadening beam encompasses a large variability of DSDs. The resulting DSD profile is used to simulate the corresponding profile of radar measurements at C band. Rainfall algorithms based on polarimetric radar measurements were taken into account to estimate the rainfall into the radar beam. Finally, merit factors were used to achieve a quantitative analysis of the performance of the rainfall algorithm in comparison with the corresponding measurements at the ground obtained from a 2D video disdrometer (2DVD) that was positioned beside the micro rain radar. In this method, the behavior change of the merit factors in the range is directly attributable to the DSD variability inside the radar measurement volume, thus providing an assessment of the effects due to beam broadening.

1. Introduction

Monitoring of precipitation over a catchment area is an important stage in many hydrological applications. In this context, weather radar offers a unique mean of characterizing rainfall variability over a range of scales and with the space–time resolutions required for a large variety of hydrological problems.

The increased interest in polarimetric radar (see Bringi and Chandrasekar 2001) in recent years has been somewhat related to the fact that polarization diversity can reduce the effect on radar precipitation estimates caused by drop size variability, allowing progress on radar rainfall estimation and on its hydrometeorological applications.

The characteristics of polarization diversity measurements in rain are governed by the shape and size distribution of raindrops. These effects, in turn, are embodied in radar measurements of the reflectivity factor (usually at horizontal polarization Z_h), differential reflectivity Z_{dr} (the ratio between reflectivities at horizontal and vertical polarizations), and specific differential phase shift K_{dp} (the difference between the phases of the radar signals at orthogonal polarizations per unit distance).

Based on the above three measurements, a number of algorithms have been developed to estimate rainfall (e.g., Sachidananda and Zrnić 1987; Chandrasekar et al. 1990; Gorgucci and Scarchilli 1997; Gorgucci et al. 2001; Ryzhkov et al. 2003; Cifelli et al. 2011). These algorithms were derived assuming equilibrium raindrop shapes determined by surface tension forces and hydrostatic and aerodynamic pressures due to airflow around the raindrop. In the literature, several shape–size relationships have been proposed to describe the shape of a raindrop (e.g., Beard and Chuang 1987; Brandes et al. 2002).

Radar measurements are always affected by errors arising from different sources of uncertainty that result

Corresponding author address: Eugenio Gorgucci, Istituto di Scienze dell'Atmosfera e del Clima, CNR, Area di Ricerca Roma-Tor Vergata, Via Fosso del Cavaliere, 100-00133 Rome, Italy.
E-mail: e.gorgucci@isac.cnr.it

DOI: 10.1175/JHM-D-14-0084.1

in a misrepresentation of the rainfall field in the spatial and temporal domains. From an operational point of view, errors and uncertainty in radar rainfall estimates result both from errors in basic polarimetric measurements and from the process of retrieving the rainfall estimation falling to the ground using relationships based on the above three radar measurements. The main causes of errors in the translation from radar measurements to rainfall can be approximately classified into three categories (Zawadzki 1984): 1) random errors related to radar signal noise, statistical sampling variability, advection and drop sorting, drop size distribution (DSD), coalescence, breakup, and evaporation; 2) systematic errors that could arise from biases in azimuth and elevation angles, calibration biases, dry and wet radome effects, ground clutter, partial beam blocking, and propagation effects; and 3) range-dependent errors, which are mainly caused by beamwidth, beam tilting, Earth curvature, beam broadening with distance, and sampling of precipitation at increasing altitude. In this context, the presence of a bright band as well as a complex topography can further increase errors affecting radar rain measurements.

The errors listed in the third category are mainly determined by the characteristics of the antenna, which defines the intrinsic features of the radar beam and propagation geometry. As the distance from the radar site increases, the radar sampling volume increases with the square of the range. Precipitation intensities often vary widely on small scales, and consequently, this progressive beam broadening makes it more unlikely that a radar measurement volume is homogeneously filled by hydrometeors. Under these conditions, the drop size distribution cannot be considered uniform within the radar sampling volume, and this situation will affect the corresponding rainfall radar measurements. Ryzhkov and Zrnić (1998), Gosset (2004), and Ryzhkov (2007) showed that for a horizontal scanning antenna the largest impact of nonuniform beam filling is on the differential phase and cross-correlation coefficient. Therefore, with the increase of gradients inside the measurement volume, the radar measurements are affected in different ways, and consequently, the rainfall estimates obtained by different algorithms will be affected differently.

The purpose of the present study is to investigate the effects due to beam broadening on the polarimetric measurements of rainfall using DSD profiles obtained by a micro rain radar (MRR) installed in the historic center of Rome during the special observation period of the Hydrological Cycle in the Mediterranean Experiment (HyMeX SOP1).

The paper is organized as follows. In section 2, the dataset of rainfall events is presented, along with a description of the meteorological conditions also revealed by weather radars. Section 3 presents the methodology used to transform DSD vertical profiles into measurement profiles collected by a ground weather radar. Data analysis, results, and discussion are presented in section 4, and the important findings of this study are summarized in section 5.

2. Dataset

The data used in this paper were collected in central Italy during the HyMeX SOP1 that took place from September to November 2012.

a. The HyMeX SOP1 in central Italy

In the Mediterranean basin, the occurrence of major natural risks related to the water cycle such as intense precipitation and flash flooding is higher during the fall season, when large thermal gradients may occur between a sea that is still warm and the cooler overlying atmosphere. The international HyMeX project aims at a better understanding and quantification of the water cycle in the Mediterranean, with an emphasis on intense rainfall events. The region under study was divided into three target areas: northwest, Adriatic, and southeast. Within each target area several hydrometeorological sites for heavy rainfall and flash flooding have been set up. Because of its central position in the Mediterranean basin, Italy is affected by weather phenomena coming from the Atlantic Ocean as well as from Siberia. For this reason, a hydrometeorological site of the HyMeX SOP1 was hosted in central Italy (CI; Ferretti et al. 2014). The region, which includes the Roman urban area, is characterized by a complex orography going from sea level to the Apennine heights and is crossed by many rivers, including the Aniene–Tiber basin and the Aterno–Pescara basin, located on the west and east sides of the Apennines, respectively.

b. Instrumentation

The CI hydrometeorological site is equipped with permanent and operational instrumentation operated by scientific and operational communities. These include instruments routinely operated by local partners contributing to SOP1, such as the dual-polarization radar Polar 55C of the National Research Council (CNR), located 15 km southeast of Rome, and the weather radar of the University of L'Aquila, placed on the top of Monte Midia at 61 km east-northeast of Rome. Under a specific agreement, further instrumentation, including the K-band MRR and a 2D video disdrometer (2DVD) used in this study, was provided by NASA GSFC and deployed to support the campaign as part of the Global Precipitation Measurement (GPM) mission

TABLE 1. List of the chosen rain events identified by a number of four digits representing the month and the day (case study), number of rainy minutes (time), 2DVD rain accumulation (ΣRG), and heights above ground level of 0°C isotherm at 0000, 1200, and 2400 UTC estimated from LIRE (15 km south of Rome).

Case study	Time (min)	ΣRG (mm)	0000 UTC (m)	1200 UTC (m)	2400 UTC (m)
0913	294	14.0	3529	3195	2680
0914	395	7.0	2680	2952	3014
0930	416	10.0	3877	3563	3670
1015	161	17.0	2880	2809	2771
1026	232	10.0	3290	3542	3019
1031	853	27.0	2360	2806	2572

prelaunch activity [see Ferretti et al. (2014) for a complete overview of observations, instruments, and models involved].

The MRR and the 2DVD used in this study were installed in Rome on the roof of the Department of Information Engineering, Electronics and Telecommunications, Sapienza University of Rome, in the heart of downtown close to the Coliseum and the Roman Forum. The two instruments were positioned side by side.

The MRR is a continuous wave frequency modulation (CWFM) radar rain profiler (Klugmann and Richter 1995) operating at K band with a low-power solid state transmitter and a 60-cm offset antenna. The radar has an integrated transmitter and receiver based on the homodyne principle. Practically speaking, in the mixing diode, the backscattered radiation produces two different frequencies with a shift that depends on the distance of the target from the radar and on the fall velocities of the particles. The vertical Doppler spectrum reproduced by the vertical fall velocity distribution of hydrometeors can be converted into drop size spectra, liquid water contents, and rain rates under the assumption of zero vertical wind.

The 2DVD (Schönhuber et al. 1997) works on the basis of two video cameras. The falling particles that cross the perpendicular common fields of view are recorded at a resolution better than 0.2 mm. The device is provided with specific software that can estimate rain rate, vertical velocity, and size and oblateness of droplets from the images.

To allow quantitative measurements, the MRR was calibrated by removing the mean bias. The calibration factor was found by adjusting the second gate Rayleigh reflectivity, computed from the corresponding MRR-derived DSD parameters, until the mean difference with the computed reflectivity from the 2DVD was zero.

c. Rain events

The study was performed using drop size spectra profiles collected by the MRR with a time resolution of 1 min together with the corresponding data collected by the 2DVD during six rainfall events that passed through the area observed by the two devices. The case studies were chosen on the basis of having significant rainfall exceeding 5 mm. Table 1 shows the selected rain events identified by four-digit numbers representing the month and the day (case study), the number of rainy minutes (time), the 2DVD rain accumulation (ΣRG), and the height above the ground level of the 0°C isotherm at 0000, 1200, and 2400 UTC estimated from the sounding station of Pratica di Mare (known as LIRE; 15 km south of Rome). For the sake of completeness, the main features characterizing rainfall events in terms of meteorological situation and storm morphology characteristics are summarized below.

Case study 0913. As a result of North Atlantic air entering the Mediterranean Sea, a low pressure area was formed over the central western basin that dropped heavy rainfall over the urban area of Rome. From 1000 to 2100 UTC, weather radars showed a series of storms crossing the covered area and dumping heavy rain. Between 1500 and 1700 UTC, a thunderstorm swept through the entire urban area of Rome and the area covered by the MRR.

Case study 0914. The same low pressure area as 0913 moved toward the regions of the middle and southern Adriatic Sea. The bad weather conditions that prevailed during the first half of the day generated widespread rainfall that hit the city of Rome. From early in the morning until 1800 UTC, the area within Polar 55C coverage was affected by storms that produced heavy widespread rainfall.

Case study 0930. A synoptic low pressure system centered on the southwest of Sardinia and moving northeast directly affected the central Italian region with widespread rainfall. Between 1400 and 2300 UTC, radar reported heavy widespread rainfall over the city of Rome.

Case study 1015. The intrusion of cold Atlantic air over the warm Mediterranean basin generated instability and a low pressure area formed over the northern Mediterranean Sea. These conditions generated storms with heavy rainfall. From 0000 to 0500 UTC, a squall line moved from west to east into the area covered by the Polar 55C, followed by

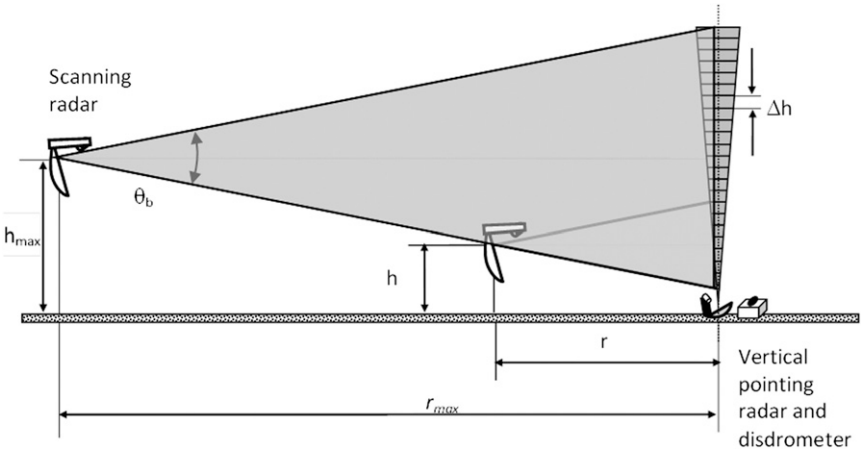

FIG. 1. Graphical depiction of the methodology used to transform DSDs provided by vertically pointing MRR to a profile as if collected by a ground-based horizontally scanning radar.

showers from cumulus clouds. From 1300 UTC, a new squall line moved eastward inside the area of radar coverage, and between 1700 and 1820 UTC a heavy rainstorm occurred over the city. Around 1900 UTC, the storm began to take on the characteristics of widespread clouds.

Case study 1026. In relation to the eastward progression of a relatively deep trough extending from the Atlantic over the western Mediterranean Sea, and to the organization of a strong warm advection at low levels from the southeast, very perturbed weather conditions developed and progressed from France to Italy across southern Spain, Corsica, and Sardinia. Heavy precipitation occurred over Lazio during the afternoon and evening. From 1200 to 1600 UTC, the development of cumulonimbus clouds occurred inside the area of radar coverage that marginally affected the city of Rome. After that, large rainbands began to entirely cover the area observed by the radar. Growing cells embedded within this wide storm produced large amounts of precipitation in the southwest quadrant of the radar coverage area.

Case study 1031. A trough extended from the Atlantic over the western Mediterranean Sea, associated with a low pressure over the Gulf of Lion, leading to strong instability involving central Italy in the afternoon. For most of the day, radar images showed rainfall from stratiform clouds with some embedded convection.

From the above, it follows that the dataset from the selected rainfall events is essentially composed of DSDs from convective clouds with a few cases of stratiform conditions. The only exception is represented by the 1031 rain event, which mainly originated from more autumnal conditions marked by, among other things, a lower melting level (Table 1).

3. Methodology

A methodology has been developed to transform estimated DSDs provided by MRR to a profile as if collected by a ground-based, horizontally scanning polarimetric radar. Figure 1 provides a graphical depiction of the procedure. Assuming a circular beam with a 1° beamwidth θ_b, the simulated radar measurement volume is supposed to be filled by contiguous 35-m-thick layers given by the range gate spacing Δh of the MRR. The layer widths are determined by their position in the radar beam. The length of each layer is defined by the pulse duration. Every minute, each layer is uniformly filled with raindrops following the DSD retrieved at the same height by the MRR. A ground-based radar placed at a certain distance from the MRR would have, above the MRR, a beam whose width is defined by such distance and will contain a fixed number of range bins of the MRR. If the radar is moved farther, the beam over the MRR gets wider and will contain more range bins of the MRR. Hypothetically speaking, if a radar system would move away from the MRR profile (e.g., at range r) and simultaneously rise at height h from the ground by an amount equal to the increase of the beamwidth related to the distance variation, a synthetic beam could be generated whose power will depend on the DSD measured by the MRR. In doing so, the elevation angle of the radar antenna would be constantly equal to 0° at each distance. Varying the distance between radar and MRR, this simulated beam would present the peculiarity of having its lower edge at a constant height from the ground. Discarding the first range bin of the MRR

profile (because it is unreliable), the height of the MRR measurements ranges between 70 and 1080 m, which can be included in a simulated 60-km range beam profile as collected by a ground-based radar. Another characteristic of these profiles is that the first radar volume in range is filled with a uniform DSD as a result of being made up of a single MRR layer.

a. Background

Because of radar beam geometry, each layer within the beam will weigh differently with the distance, so the different DSDs will have a different weight in the beam. At a fixed range, the weight of each layer in the radar measurement volume is defined by the beam-weighting function. Varying the range, a synthetic DSD profile can be generated by the composition of all the different DSDs measured by the MRR filling the radar measurement volume. It follows that the radar sample volume will contain nonuniform rain obtained directly from experimental measurements.

In this context, the different vertical layers that are simulated by the scanning radar are filled with precipitation having different DSDs. The precipitation can be described by a gamma DSD given by

$$N(D) = N_0 D^{\mu} \exp(-\Lambda D), \tag{1}$$

where $N(D)$ is the number of raindrops per unit volume per unit size in the interval $(D, D + \Delta D)$ and N_0 ($\mathrm{mm}^{-1}\,\mathrm{m}^{-3}$), Λ (mm^{-1}), and μ are the intercept, shape, and slope parameters of the gamma DSD, respectively. The relation between Λ, D_0, and μ is given by

$$\Lambda D_0 = 3.67 + \mu, \tag{2}$$

where D_0 is the drop median volume diameter. Therefore, each layer contained in the radar volume is described by different (N_0, D_0, μ) triplets.

This nonuniform distribution of precipitation in the radar measurement volume in conjunction with the antenna radiation pattern will affect the corresponding radar measurements differently than those involving a uniform distribution of precipitation. In fact, the radiation pattern depending on the beam field variation as a function of the spherical coordinates θ and φ assigns different weights to each layer. Antenna radiation gain $G(\theta, \varphi)$ has been assumed to be axisymmetric with respect to the boresight direction and with a Gaussian shape of the beam-weighting function (Doviak and Zrnić 1993). For each layer illuminated by the radiation pattern, the corresponding beam-weighting function W_i has been found under the assumption that the boresight direction of the 3 dB antenna pattern width is perpendicular to the plane containing the layers, such as

$$\iint G^2(\theta, \varphi)\, d\Omega \approx \sum_{i=1}^{N_L} W_i, \tag{3}$$

where $d\Omega$ is the elemental solid angle and N_L the number of layers illuminated by the two-way antenna power pattern.

Taking into account the individual DSD of each layer, the composition performed by the beam-weighting function gives the following DSD:

$$N(D) = \sum_{j=1}^{N_L} W_j n_j(D), \tag{4}$$

where $n_j(D)$ is the number of raindrops per unit volume per unit size in the interval $(D, D + \Delta D)$ of the jth layer. This can be obtained by finding for each class of diameter interval the weighted value of the corresponding spectral drop densities. The bins of the spectral drop density provided by the MRR vary with height, and it is convenient to convert all the spectral densities to have the same bins. This was achieved by finding mean bins for the dataset and then resampling each spectral density by linear interpolation.

To obtain gamma DSD parameters from MRR spectra, the method of moments is used (Tokay and Short 1996). In general, for the gamma DSD model, the xth moment is defined as

$$M_x = N_0 \frac{\Gamma(\mu + x + 1)}{\Lambda^{\mu + x + 1}} = \int_{D_{\min}}^{D_{\max}} N(D) D^x\, dD, \tag{5}$$

where $D_{\min}$ and $D_{\max}$ are the minimum and maximum diameter obtained from the MRR measurements. The three parameters that unambiguously determine a gamma DSD (N_0, D_0, μ) can be obtained from any three moments, such as the third, fourth, and sixth, as in Tokay and Short (1996). The ratio F given by

$$F = \frac{(M_4)^3}{(M_3)^2 M_6}, \tag{6}$$

can be used to calculate μ:

$$\mu = \frac{11F - 8 + \sqrt{F(F + 8)}}{2(1 - F)}, \tag{7a}$$

with D_0 and N_0 given by

$$D_0 = \frac{3.67 + \mu}{\mu + 4} \frac{M_4}{M_3} \tag{7b}$$

and

$$N_0 = \frac{\Lambda^{\mu+4} M_3}{\Gamma(\mu+4)}. \quad (7c)$$

MRR spectra exhibiting aliasing (Tridon et al. 2011) were not considered for processing and discarded in the subsequent analysis.

The radar observables Z_h, Z_{dr}, and K_{dp} can be expressed in terms of the DSD as follows (Bringi and Chandrasekar 2001):

$$Z_{h,v} = \frac{\lambda^4}{\pi^5 |K_w|^2} \int \sigma_{h,v}(D) N(D)\, dD \quad (\mathrm{mm^6\,m^{-1}}), \quad (8)$$

where $\sigma_{h,v}$ refers to the backscatter cross section of raindrops at horizontal h and vertical v polarization, λ is the wavelength, and K_w is the dielectric factor of water. The ratio of (Z_h/Z_v) defines the differential reflectivity, commonly expressed in logarithmic scale as

$$Z_{dr} = 10\log(\xi_{dr}) = 10\log\left(\frac{Z_h}{Z_v}\right) \quad (\mathrm{dB}). \quad (9)$$

The specific differential propagation phase can be defined as

$$K_{dp} = \frac{180\lambda}{\pi} \int \mathrm{Re}[f_h(D) - f_v(D)] N(D)\, dD \quad (^\circ\,\mathrm{km^{-1}}), \quad (10)$$

where f_h, and f_v are the forward-scattering amplitudes at h and v polarization, respectively.

b. Simulation of polarimetric radar profiles

The dataset consists of synthetic horizontal profiles where in each range gate the gamma raindrop size distribution is fixed by the MRR measurements. These DSD profiles correspond to a 60-km-long path containing 800 range bins spaced by 0.075 km. Each profile presents the special feature of having a constant rainfall rate at the ground at all distances while the DSD changes because of the broadening of the radar beam with range and to the vertical gradient in the radar resolution volume. In each range gate, the DSD profile is used to simulate the corresponding Z_h, Z_{dr}, and K_{dp} profiles of radar measurements at 5.6 GHz (C band). The procedure is based on T-matrix and Mueller-matrix scattering models (Waterman 1965; Vivekanandan et al. 1990). In the simulation, the Beard and Chuang (1987) relation is assumed for the drop shape while the drops are canted with the mean canting angle equal to 0° and the width of the canting angle distribution equal to 10°. Temperature is assumed to be 20°C. Moreover, differential phase on backscattering is added to the path

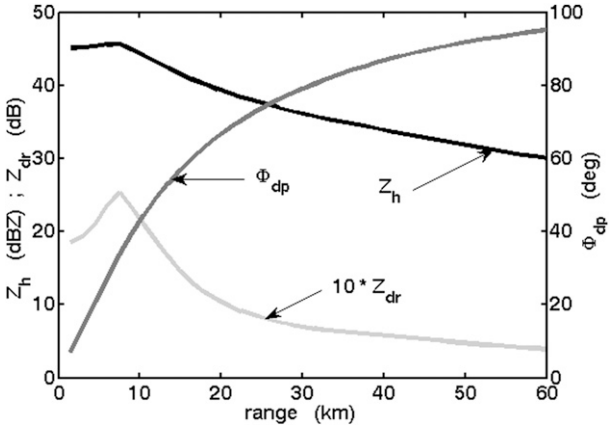

FIG. 2. Synthetic range profiles of Z_h, Z_{dr}, and Φ_{dp} radar measurements obtained by a C-band weather radar with an antenna of 1° beamwidth. The radar volume was obtained by 35-m-layer fill with uniform DSD corresponding to the DSD estimated by the MRR at the same height.

differential phase, and for each rain profile, cumulative attenuation and differential attenuation are computed in each range bin. The attenuated Z_h and Z_{dr} profiles are obtained by subtracting attenuation and differential attenuation from the corresponding intrinsic values. Figure 2 shows an example of synthetic range profiles of Z_h, Z_{dr}, and Φ_{dp} radar measurements obtained by a C-band weather radar with a 1° beamwidth antenna.

A number of algorithms have been introduced in the literature for rainfall estimation using radar measurements obtained from polarization diversity radar operating in linear polarization basis. The most widely used algorithms can be broadly classified into three categories: 1) algorithms that use reflectivity factor R_z, 2) algorithms that use reflectivity and differential reflectivity R_{dr}, and 3) algorithms that use differential propagation phase R_{dp}. In this study, it was decided to find radar rainfall algorithms for C band for widely varying drop size distributions. This was obtained by randomly varying the parameters of the normalized gamma distributions ($0.5 \le D_0 \le 3.5$ mm, $3 \le \log_{10} N_w \le 5$, $-1 < \mu \le 4$ for $R < 200\,\mathrm{mm\,h^{-1}}$ and $Z_h < 55$ dBZ). In this way, the algorithms provide a performance reference for evaluating the precipitation variability of the individual events. The algorithms are as follows:

$$R_z = 4.38 \times 10^{-2} Z_h^{0.603} \quad (\mathrm{mm\,h^{-1}}), \quad (11a)$$

$$R_{dr} = 6.61 \times 10^{-3} Z_h^{0.911} \xi_{dr}^{-2.56} \quad (\mathrm{mm\,h^{-1}}), \quad (11b)$$

and

$$R_{dp} = 19.52 K_{dp} \quad (\mathrm{mm\,h^{-1}}). \quad (11c)$$

For radar operating at attenuated frequencies, attenuation due to precipitation may degrade the radar measurement whose amount becomes, to a considerable, degree dependent on the precipitation path. Attenuation and differential attenuation cumulatively increase with range and may affect precipitation estimates at distances far from the radar site. Therefore, attenuation, differential attenuation, and the presence of backscatter differential phase δ should be taken into account when evaluating the performance of R_z, R_{dr}, and R_{dp} at C band. These effects due to propagation are mainly caused by the attenuation of Z_h and by the differential attenuation of Z_{dr} together with the presence of the differential backscatter phase.

In this study, the attenuation correction procedure based on the differential propagation phase (Bringi et al. 1990) is used:

$$\alpha_h = 6.6 \times 10^{-2} K_{dp} \quad (\mathrm{dB\,km^{-1}}) \tag{12a}$$

and

$$\alpha_{dp} = 1.7 \times 10^{-2} K_{dp} \quad (\mathrm{dB\,km^{-1}}). \tag{12b}$$

Equations (12a) and (12b) were obtained by the above-mentioned simulation method.

To analyze the behavior of the algorithms R_z, R_{dr}, and R_{dp} in the presence of beam broadening along a distance of 60 km, a dataset consisting of profiles of Z_h, Z_{dr} not attenuated and attenuated, together with Φ_{dp} unaffected and affected by the differential phase upon backscatter, was built directly from the in situ observation of the spectral hydrometeor density given by the MRR.

A profile is generated each time precipitation is present at the same time on the ground and on each range bin of the MRR. The profiles have a nominal time resolution of 1 min.

It is necessary to emphasize that this methodology originates profiles in which the measurements in a range bin are related to those of the previous ones as a consequence of the layers that they share. From a practical viewpoint, the synthetic range profiles of Z_h, Z_{dr}, Φ_{dp}, A_h, and A_{dp}, reflecting the methodology used to generate them, cannot be generalized to real situations.

4. Data analysis, results, and discussion

To achieve a quantitative analysis of the rainfall algorithm performances and their behavior with the increasing size of the radar measurement volume, three merit factors were taken into account: 1) the normalized standard error (NSE), defined as the root-mean-square error normalized to the mean of the ground reference measurements:

$$\mathrm{NSE} = \frac{\left[\frac{1}{n}\sum_{i=1}^{n}(R_i - G_i)^2\right]}{\left(\frac{1}{n}\sum_{i=1}^{n} G_i\right)}, \tag{13}$$

where n is the number of paired variables, R_i is the synthetic radar rainfall estimate, and G_i is the ground reference; 2) the normalized bias (NB) defined as the mean difference normalized to the mean of the ground reference measurements:

$$\mathrm{NB} = \frac{\left[\frac{1}{n}\sum_{i=1}^{n}(R_i - G_i)\right]}{\left(\frac{1}{n}\sum_{i=1}^{n} G_i\right)}, \tag{14}$$

where a negative value of NB means an underestimation by the synthetic radar; and 3) the correlation coefficient to measure the strength of a linear relationship between R_i and G_i measurements defined as

$$\rho = \frac{\left[\frac{1}{n}\sum_{i=1}^{n}(R_i - \overline{R})(G_i - \overline{G})\right]}{\left[\frac{1}{n}\sum_{i=1}^{n}(R_i - \overline{R})^2\right]^{1/2}\left[\frac{1}{n}\sum_{i=1}^{n}(G_i - \overline{G})^2\right]^{1/2}}. \tag{15}$$

In particular, the analysis of the correlation coefficient trend in distance provides a direct indication of the decorrelation between radar and ground measurements introduced by beam broadening.

a. Rain event analysis

Figure 3 shows normalized standard errors between the 1-min rain rates from the 2DVD measurements and the corresponding C-band radar-derived rainfall estimates obtained using 1) R_{DSD} (rainfall rate computed by integration of the MRR-derived DSD filling the antenna beam), 2) R_z, 3) R_{dr}, and 4) R_{dp} algorithms, as a function of the range. NSE is reported on an event-by-event basis to show the wide range of rainfall variability among the different events. Figure 3a shows NSE between the rain computed using the DSD directly inside the radar measurement volume and the 2DVD rainfall measurements. The wide variability of NSE for the different events is not surprising because the comparison is obtained by relating the 2DVD and the MRR measurements at each minute without any shift between the two estimates. With the exceptions of the 0914 and 1026 events, the common feature of NSE is to

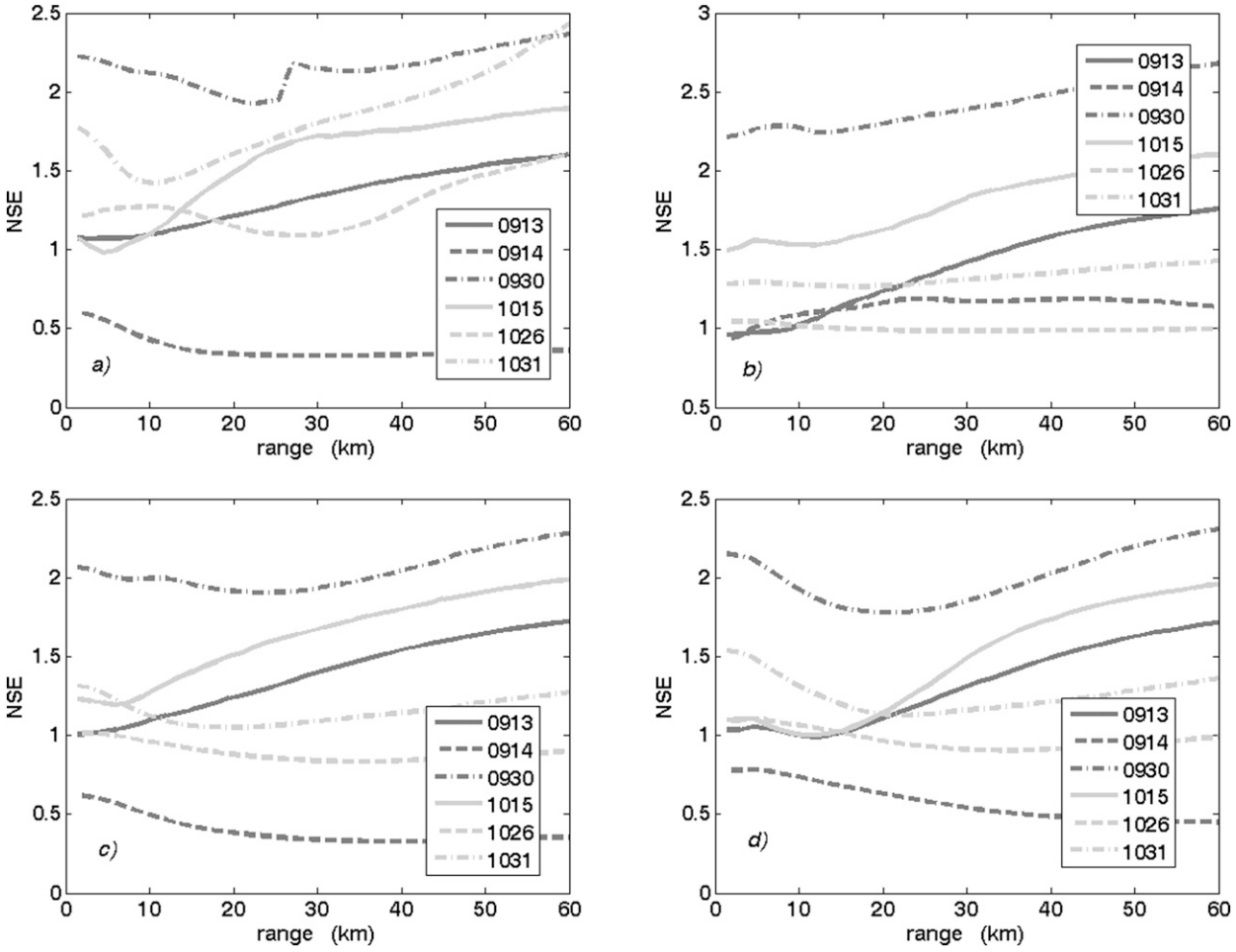

FIG. 3. NSE between 1-min rain rates from the 2DVD disdrometer and the corresponding C-band radar-derived rainfall estimates using (a) R_{DSD}, (b) R_z, (c) R_{dr}, and (d) R_{dp} algorithms as a function of the range. NSE is reported on an event-by-event basis to show the wide range of rainfall variability. Note that the *y*-axis range changes.

increase with increasing range as a result of beam broadening.

Figure 4 shows the NB between the 2DVD rainfall measurements and the corresponding C-band radar-derived rainfall estimates obtained using 1) R_{DSD}, 2) R_z, 3) R_{dr}, and 4) R_{dp} algorithms. The most important aspect highlighted by Fig. 4 is that the NBs of R_{dr} and R_{dp} show patterns very similar to that of R_{DSD}, detecting a marked ability to follow the variability of the different rain events and displaying NBs very close to zero, on average. The same is not true for the NBs of R_z, which show a wide variability for the different events, giving, on average, an overestimation.

Although the merit factors obtained with the different algorithms show differences among them, the variability among the different rainfall events is so high in range that it is not possible to capture a general trend. Nevertheless, although comparison between modeled radar and ground rainfall is based on the basic assumption that the precipitation observed aloft impacts the surface directly below the volume sampled by the radar, in practice there are a number of factors that limit this assumption, including the presence of horizontal wind that pushes the rain off the vertical. In addition, the high variability is also caused by different statistical characteristics of intensity, duration, and type of rainfall. It should be noted that the precipitation events considered in this study consist of storm cases associated with convective or stratiform systems. During the course of the events, the convection often occurs in association with stratiform conditions, making the boundary between the two rain types less distinct. Under these conditions, the variability of the mean rain intensity is generally smoothed. To more fully generalize the different conditions, the analysis was conducted for short-duration

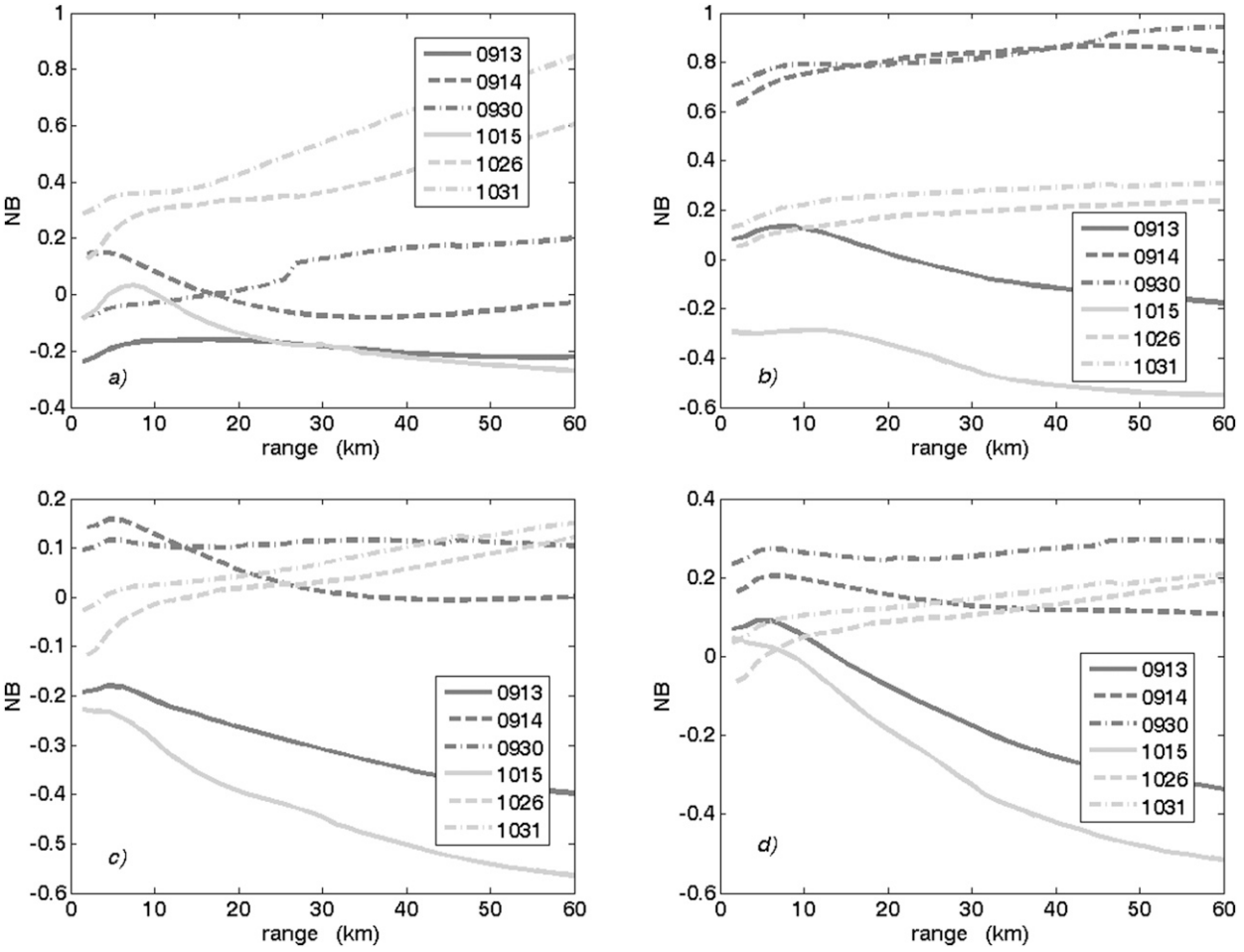

FIG. 4. As in Fig. 3, but for NB.

storms, which ensures a wide variability of precipitation characteristics.

b. 1-min rainfall analysis

To consider the temporal structure and evolution of the rainfall produced by the different rain cells and their influence on the rainfall estimation, a short-term analysis was performed. Consecutive 60-min intervals of rainfall were separated into individual rainfall events. This methodology allows for generalization of the range trend of merit factors for a wide variety of types of precipitation by setting for each distance the mean statistics with the corresponding variability interval. The procedure is as follows:

- Individual single rainfall events were made by selecting randomly one of the six precipitation cases and a starting time from which 60 min of consecutive precipitation can be taken.
- Two events were selected if they overlap for less than 30 min.
- The corresponding range radar profiles were selected.
- For each 60-min rain event, merit factors between ground and modeled radar rainfall estimates were computed using the different algorithms.
- Mean values and 95% confidence intervals of merit factors were obtained from 100 different rain events.

Table 2 shows the 95% confidence interval and the mean value of the merit factors NSE, NB, and ρ between the 1-min rainfall rate derived from the 2DVD and the corresponding ones computed for the lower MRR range bin using R_{DSD}, R_z, R_{dr}, and R_{dp} algorithms for 60-min rain events. The lower MRR range bin used in this study was centered at 70 m (second range gate) and is called the reference level (RL). Also in this comparison, no time shift has been introduced between 2DVD and MRR measurements. Variable R_{DSD} is the rainfall rate computed from the MRR-derived DSD at RL, and therefore, the relative merit factors represent the rainfall variability between the measure on the ground and at 70 m above ground. The mean NSE of R_{dr} is very close to the one of

TABLE 2. The 95% confidence interval and the mean value of merit factors NSE, NB, and ρ between 1-min rainfall rate derived from the 2DVD and the corresponding ones computed for the lower MRR range bin using R_{DSD}, R_z, R_{dr}, and R_{dp} algorithms for 60-min rain events.

	R_{DSD}			R_z			R_{dr}			R_{dp}		
	5%	Mean	95%	5%	Mean	95%	5%	Mean	95%	5%	Mean	95%
NSE	0.32	0.68	1.11	0.45	0.90	1.54	0.29	0.67	1.13	0.38	0.74	1.21
NB	−0.28	0.03	0.32	−0.25	0.45	1.21	−0.39	−0.01	0.28	−0.46	0.03	0.31
ρ	0.48	0.74	0.92	0.42	0.75	0.93	0.45	0.75	0.92	0.44	0.75	0.92

R_{DSD} while R_z shows the worst, as is expected from the theory. The mean NBs of R_{dr} and R_{dp} have very small values and are comparable to R_{DSD}, whereas R_z presents an overestimation of 45%. Correlation coefficients of the different algorithms are comparable to that of R_{DSD}.

Increasing the distance, the radar beam will contain a greater number of MRR range gates, and in the presence of gradients, the different parameters of the synthetic radar beam will differ from those related to the RL. This additional variability will affect the merit factors.

Figure 5a shows the mean NSE between a 1-min rainfall rate derived from the 2DVD and the corresponding radar rainfall estimates obtained from R_z, R_{dr}, and R_{dp} algorithms, as a function of the range. The solid thin lines with the same colors represent the upper and lower bounds of the 95% confidence intervals for the three algorithms. The mean NSE of R_{dr} and R_{dp} show values that are substantially similar to each other and, on average, 30% lower than those of R_z. The combined effect of beam broadening and gradients is summarized by a 15% increase of NSE for R_z at 60 km, whereas R_{dr} and R_{dp} show a trend essentially constant in the range. The upper narrow lines show a marked higher increase with distance in comparison to the corresponding mean values of NSE.

Figure 5b shows the mean NB for the three algorithms with respect to the 2DVD. It should be noted that while R_{dr} and R_{dp} exhibit little bias, R_z shows an overestimation of more than 50% and a confidence interval much wider than those related to R_{dr} and R_{dp}. Figure 5c shows the mean correlation coefficients for the three algorithms, which present a similar pattern, with the maximum value in range between 20 and 30 km and then decreasing with increasing distance. The 95% confidence intervals extend from 0.43 to 0.96.

The most significant result obtained from this analysis, shown in Table 2 and Fig. 5a, is that the mean NSEs of the different algorithms have 95% confidence intervals, for the most part overlapping each other, a condition that in part trivializes the possibility of defining the best radar rainfall algorithm.

c. *Hourly rainfall analysis*

To better characterize the different behaviors of radar rainfall estimations using R_z, R_{dr}, and R_{dp} algorithms, the 1-min rainfall data were aggregated to produce hourly cumulative rainfall. In this way, under the validity of an isotropic space–time, there is a reduction of temporal rainfall variability with a consequent greater phenomenological increase that will yield a better understanding of the different performances of the algorithms. The methodology used is as follows:

- Hourly rainfall profiles were obtained from each of 60-min rainfall events.
- Eight profiles were selected randomly from the hourly rainfall dataset to generate 8-h rain events.
- For each 8-h rain event, merit factors between ground and radar hourly rainfall estimates are computed using the different algorithms as a function of range;
- Repeating the above procedure for the entire dataset (i.e., 64 times), the mean values of merit factors and 95% confidence intervals are computed by 1-h rainfall accumulation as a function of range.

Table 3 shows the 95% confidence interval and the mean value of the merit factors NSE, NB, and ρ between 1-h rainfall accumulations of the 2DVD and the corresponding ones computed at RL using R_{DSD}, R_z, R_{dr}, and R_{dp} algorithms. In this context, the merit factors of R_{DSD} give the minimum sampling error between the two different instruments under the assumption that hourly accumulations minimize the variance between the ground and radar rainfall measurements.

From the comparison between Table 2 and Table 3, it appears evident that when considering accumulated precipitation amounts, NSE is considerably lower than about 50%. This smaller difference between radar and ground hourly precipitation measurements is also confirmed by the higher correlation coefficients for all algorithms.

Figure 6a shows an NSE between hourly rainfall measurements of the 2DVD and the corresponding rainfall estimations obtained from R_z, R_{dr}, and R_{dp} algorithms as a function of the range. The comparison between Figs. 5a and 6a also shows a significant NSE reduction of about 50% along the range for all algorithms. In addition, it should be emphasized that the variation due to beam broadening is more evident, as NSEs have an average increase of 20% along the entire

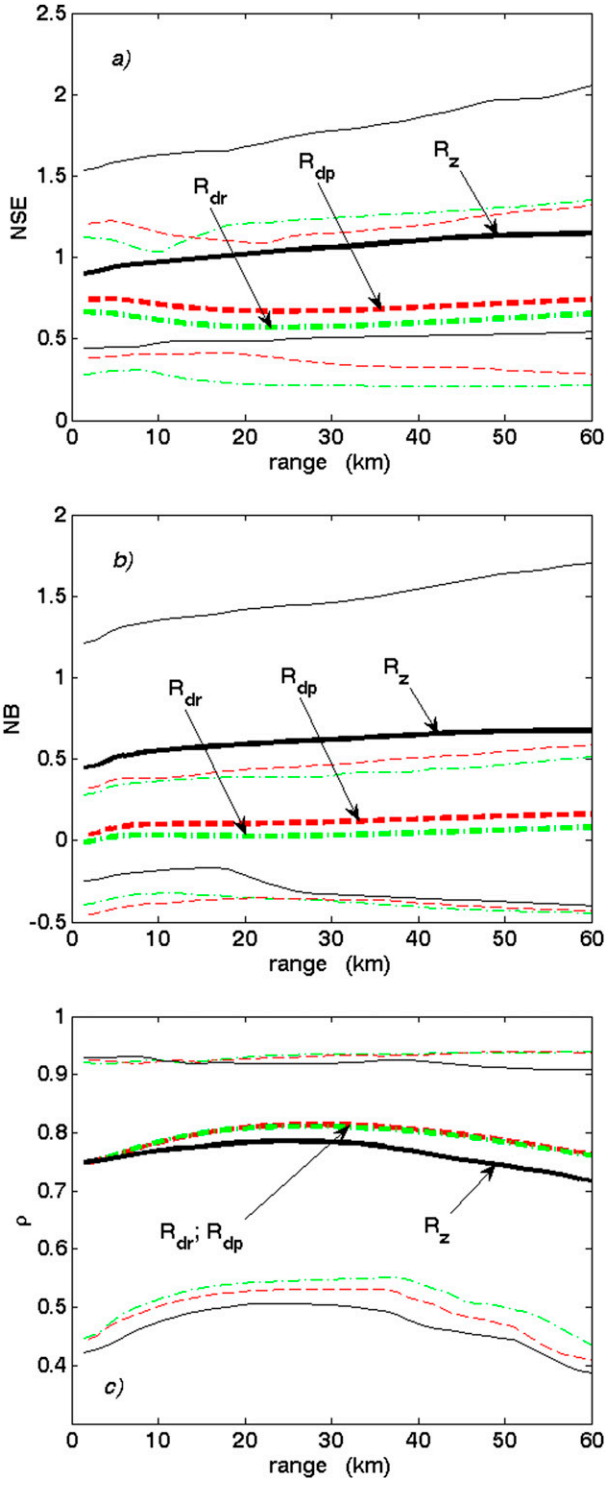

FIG. 5. Merit factors (a) NSE, (b) NB, and (c) ρ between 1-min rainfall rate derived from the 2DVD and the corresponding radar rainfall estimates obtained from R_z (thick black solid line), R_{dr} (thick green dash–dotted line), and R_{dp} (thick red dashed line) algorithms, as a function of the range. The thin lines represent the upper and lower bounds of the 95% confidence intervals for the three algorithms.

distance of 60 km for all algorithms. The comparison between Figs. 5b and 6b shows a marked reduction of the confidence intervals of the NB. The mean NBs remain constant over the range while the NBs of R_{dr} and R_{dp} are close to zero, and R_z shows a large overestimation. Figure 6c shows a significant improvement of correlation coefficients between hourly cumulative 2DVD and radar rainfall measurements with respect to Fig. 5c for all the algorithms. It is quite evident that the ρ values of R_{dr} and R_{dp} are better than R_z. In fact, while R_z varies between 0.86 and 0.64, the other two have comparable mean values ranging between 0.98 and 0.81. This improvement should not be surprising considering that the cumulative precipitation amount reduces the differences due to rainfall variability, sampling modes, instrument precision, and environmental effects.

An interesting result obtained from hourly rainfall analysis is that, although it has a significant reduction of NSE, the 95% confidence intervals of the R_z, R_{dr}, and R_{dp} algorithms have a partial overlap with each other that does not allow a definition regarding which is the best algorithm for radar rainfall estimation over the entire domain of rain variability.

d. *Practical aspects of radar rainfall estimation*

For radars operating at high frequencies (e.g., C band), attenuation due to precipitation may degrade the radar measurement by an amount that increases depending on the precipitation path. To study the behavior of the different algorithms in the presence of these effects, the attenuated Z_h and Z_{dr} profiles were generated as described in section 3.

Since Z_{dr} can be affected by nonnegligible differential attenuation, it is not possible to use relations based on this measurement to estimate δ (Scarchilli et al. 1993); in order to reduce its influence on Φ_{dp} profiles, it was necessary to apply an iterative filtering technique (Hubbert and Bringi 1995). The iterative application of this filter was designed to remove gate-to-gate fluctuations caused by δ and preserve the Φ_{dp} physically meaningful trends.

Figure 7 shows the scatter between "true" K_{dp} versus K_{dp}^{δ}, the latter obtained as the slope of a linear regression line of the filtered Φ_{dp} range profile. The scatter is characterized by having NSE = 0.46, NB = 0.03, ρ = 0.968, and a slope of 0.997.

Since attenuation and differential attenuation are linearly related to Φ_{dp} in rainfall, for each rain profile, cumulative attenuation and differential attenuation are computed in every range bin from Φ_{dp} by Eq. (12), which can be used to correct the attenuated Z_h and Z_{dr} profiles from attenuation and differential attenuation. To evaluate the performance of R_z and R_{dr} in the

TABLE 3. As in Table 2, but for the 2DVD 1-h rainfall accumulations.

	R_{DSD}			R_z			R_{dr}			R_{dp}		
	5%	Mean	95%	5%	Mean	95%	5%	Mean	95%	5%	Mean	95%
NSE	0.10	0.24	0.39	0.23	0.48	0.72	0.12	0.23	0.34	0.12	0.19	0.30
NB	−0.16	−0.02	0.16	0.06	0.33	0.68	−0.15	−0.05	0.10	−0.07	0.05	0.16
ρ	0.86	0.95	0.99	0.56	0.85	0.99	0.88	0.95	0.99	0.89	0.96	0.99

presence of propagation effects, unaffected and corrected radar measurements are taken into account.

With regard to attenuation, differential attenuation, and backscattering differential phase, their effects on rainfall estimation are presented in Fig. 8a, in which are shown the differences in NSEs between 1-h rain amounts from the 2DVD and the corresponding radar rainfall estimates using R_z and R_{dr} algorithms when radar measurements are unaffected and affected by propagation effects after the correction of attenuation as a function of the range. The combined influence of attenuation and δ on R_z and R_{dr} is described by an increase of NSE that reaches almost linearly in range, at 60 km, 9% and 3%, respectively. Following the same procedure, Fig. 8b shows the variations in NB that represent an increase of about 14% for R_z and a decrease of 5% for R_{dr}.

e. *Hourly rainfall analysis in the presence of propagation effects and measurement errors*

To better characterize the different behaviors of radar rainfall estimations using the R_z, R_{dr}, and R_{dp} algorithms in the presence of the propagation effects as well as of measurement errors, the following method was set up:

- The Z_h, Z_{dr}, and K_{dp} profiles of radar measurements referring to each 60-min rainfall event were considered.
- The Z_h^m, Z_{dr}^m, and Φ_{dp}^m profiles were obtained by subtracting attenuation and differential attenuation from the profiles of intrinsic Z_h and Z_{dr} measurements while δ was added to the Φ_{dp} profile at each range bin.
- Measurement random errors of 1 dB, 0.2 dB, and 3° were superimposed to the Z_h^m, Z_{dr}^m, and Φ_{dp}^m profiles respectively, to obtain the Z_h^{mn}, Z_{dr}^{mn}, and Φ_{dp}^{mn} measurements.
- An iterative filtering technique was applied to remove the high-frequency signal as well as to mitigate the δ effects to the Z_h^{mn}, Z_{dr}^{mn}, and Φ_{dp}^{mn} profiles, and the Z_h^f, Z_{dr}^f, and Φ_{dp}^f measurements were produced.
- The quantities Z_h^c and Z_{dr}^c were obtained by adding to Z_h^f and Z_{dr}^f, respectively, the cumulative attenuation and differential attenuation using relations based on Φ_{dp}^f.
- An hourly rainfall profile was obtained from each 60-min rainfall event computed using Z_h^c, Z_{dr}^c, and Φ_{dp}^f.
- Eight profiles were selected randomly from the hourly rainfall dataset to generate 8-h rain events.

The method continued by following the same methodology used for hourly rainfall analysis.

Figure 9a shows the mean NSE between hourly rainfall measurements of the 2DVD and the corresponding rainfall estimations obtained from the R_z (thick black line), R_{dr} (thick green dash–dotted line), and R_{dp} (thick red dotted line) algorithms using Z_h^c, Z_{dr}^c, and K_{dp}^f as a function of the range. The comparison between Figs. 6a and 9a shows a moderate increase of R_z and R_{dr} by a quantity equal to that shown in Fig. 8a. With regard to the comparison between the R_{dp} measurements, there is a significant increase, on average, by 25% along the range, which is attributable to the noise of the differential phase shift that is still present after filtering. Analyzing the mean rainfall estimations obtained with the different algorithms, it appears evident that R_{dr} presents the lowest NSE, which, on average, is less than 30% and 25% compared to the corresponding values of R_z and R_{dp}, respectively. Of course, even in the presence of propagation effects and measurement errors, hourly rainfall analysis highlights the impossibility of defining the best algorithm for the full range of rainfall variability. This is clear by observing that the upper bound of the 95% confidence interval of R_{dr} partially overlaps the lower bound of the 95% confidence intervals of R_z and R_{dp}.

Figure 9b shows the mean NB between hourly rainfall measurements of the 2DVD and the corresponding rainfall estimations obtained from the R_z, R_{dr}, and R_{dp} algorithms using Z_h^c, Z_{dr}^c, and K_{dp}^f as a function of the range. The comparison with Fig. 6b shows no major differences, with the exception of a greater variability in the range of NB corresponding to R_{dp} as a result of an increased residual noise on Φ_{dp}^f.

Figure 9c shows the mean correlation coefficient between hourly rainfall measurements of the 2DVD and the corresponding rainfall estimations obtained from the R_z, R_{dr}, and R_{dp} algorithms using Z_h^c, Z_{dr}^c, and K_{dp}^f as a function of the range. The comparison with Fig. 6b shows an overall decrease in the range of correlation coefficient for the three algorithms due to the presence of measurement errors. In particular, the

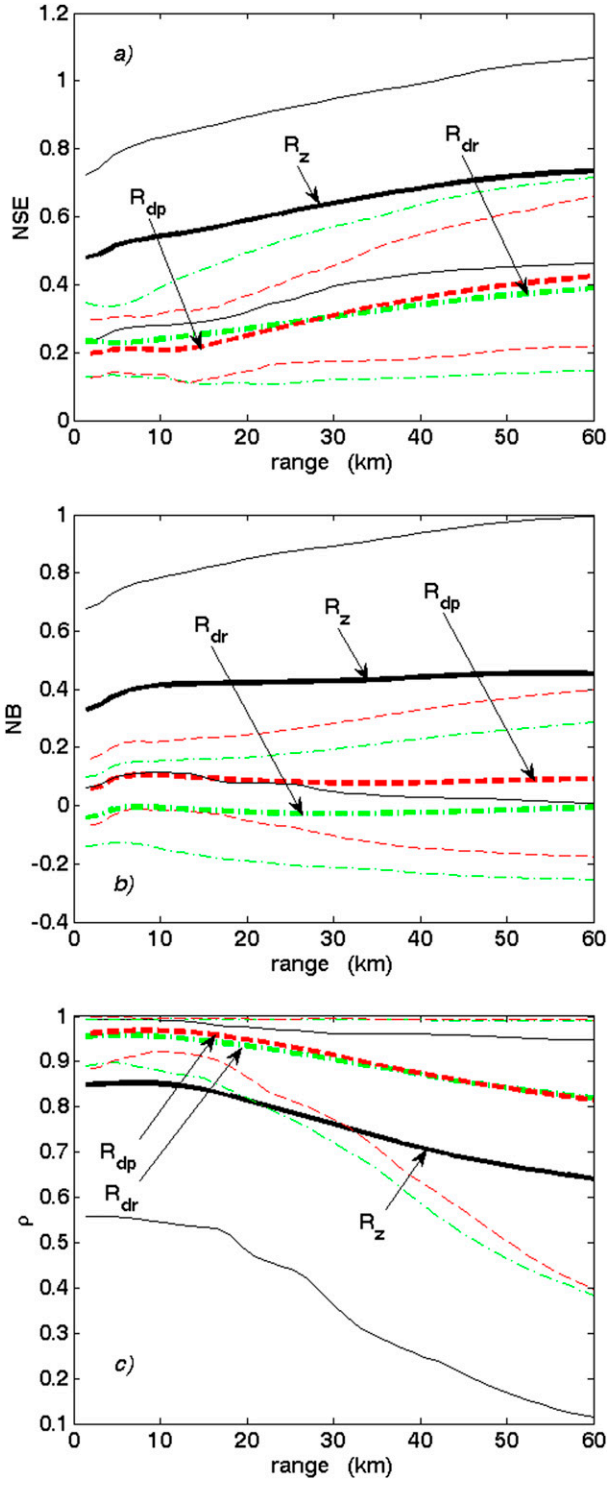

FIG. 6. As in Fig. 5, but for 1-h rain amounts and the corresponding C-band radar-derived rainfall estimates.

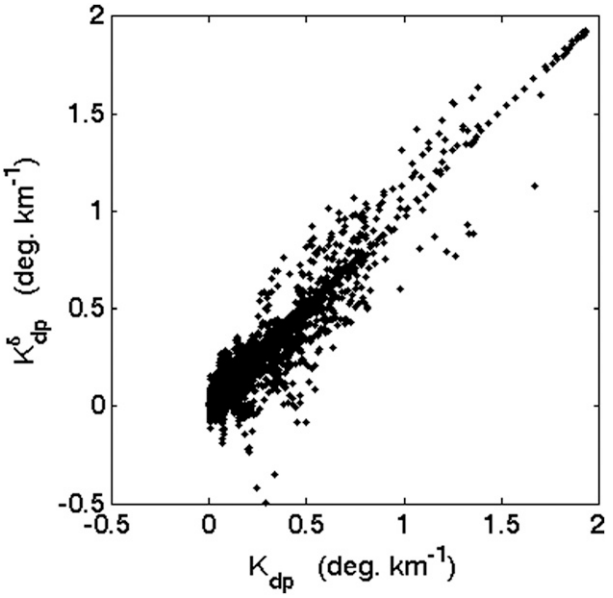

FIG. 7. Scatterplot between "true" K_{dp} vs K_{dp}^{δ} obtained as the slope of a linear regression line fit of Φ_{dp}.

correlation coefficient of R_{dp} shows a variation so wide as to be, on average, comparable to that of R_z.

5. Summary and conclusions

The quantitative estimation of rain rates using meteorological radar has been one of the main themes in radar meteorology and radar hydrology. From a theoretical point of view, the advent of dual-polarized radar techniques has made it generally possible to obtain rain algorithms less sensitive to drop size distribution variations and to improve the identification of different hydrometeor types and the knowledge of radar calibration systems as well as the way to minimize attenuation effects. While all this has been well established, from an operational point of view the problems regarding the improvement of radar rainfall accuracy essentially remain unsolved. The main reason for this limit is directly attributable to the geometry of radar measurements combined with the variability of the spatial structure of precipitation systems. On the other hand, the different evolutions of rainfall that occur in a coverage space controlled by radar are misrepresented by the rain gauge measurements usually taken to validate radar rainfall.

The purpose of the present study has been to investigate the effects due to beam broadening on the radar rainfall measurements using drop size distribution profiles obtained by a micro rain radar installed during the SOP1 of the HyMeX campaign in the downtown area of Rome. The key was to develop a methodology that would transform collected vertical DSD profiles to

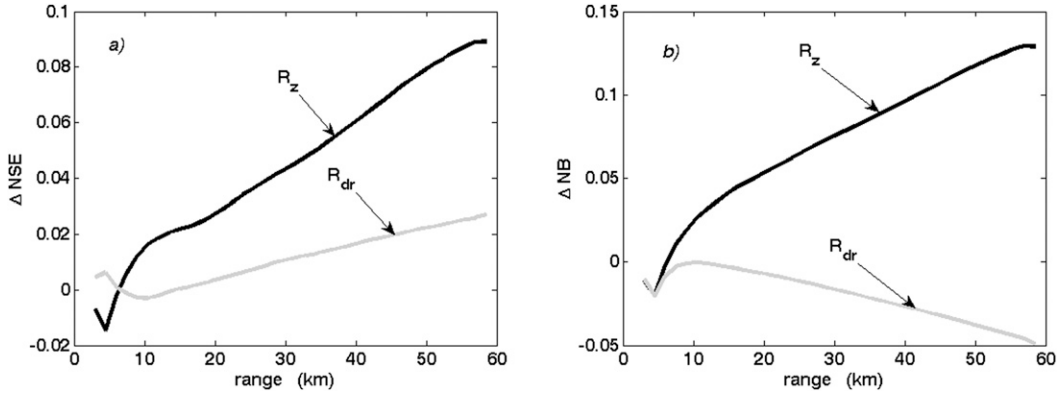

FIG. 8. Difference in (a) NSEs and (b) NBs between 1-h rain amounts from the 2DVD disdrometer and the corresponding C-band radar-derived rainfall estimates using R_z (black) and R_{dr} (light gray) algorithms when radar measurements are unaffected and affected by propagation effects as a function of the range.

range profiles simulating those collected by a ground-based polarimetric radar. A synthetic radar beam was generated with a resolution that changes as a function of range and beamwidth and presents the unique quality of having the same rainfall rate at ground. As a result, any change in range between radar and ground rainfall can be directly attributable to the effect of beam broadening and then to the variation in the range of DSDs.

To achieve a quantitative analysis of the different rainfall algorithms, merit factors such as NSE, NB, and correlation coefficients were used to assess the influence of the spatial variability between radar and ground rain rate related to the increasing size of the beam.

The analysis of the different case studies considered in this study showed a great variability from one rainfall event to another both in space and time and even within a single rainfall event, variability that did not allow for the discovery of an overall underlying trend in the range. For this reason, the entire dataset was converted to 60-min rain events from which to calculate the mean value and 95% confidence intervals of merit factors for the different algorithms.

In this context, the mean NSEs of R_{dr} and R_{dp} show values that are substantially similar to each other and on average 30% lower than those of R_z. The combined effect of beam broadening and gradients is summarized by a 15% increase of the NSE for R_z at 60 km, while those of R_{dr} and R_{dp} show an essentially constant trend in the range. However, the most significant result obtained from this analysis is that the mean NSEs of the different algorithms have 95% confidence intervals, for the most part overlapping each other, a condition that trivializes in part the possibility of defining the best radar rainfall algorithm.

To further reduce the differences between radar measurements and measurements occurring at the ground because of different sampling modes, instrument precision, and environmental effects, the 1-min rainfall data were aggregated to produce hourly cumulative rainfall. Under these conditions, for all algorithms, the NSE shows a significant reduction of about 50% while a more marked trend is highlighted by an increase of about 20% along the entire distance of 60 km that can be directly attributable to the beam broadening.

Since the study aimed to evaluate the beam-broadening effects on radar rainfall algorithms that use C-band polarimetric radar measurements, propagation effects were considered. The overall result of these effects on R_z and R_{dr} is described by an increase of NSE that in range almost linearly reaches, at 60 km, 9% and 3%, respectively.

Finally, for a complete error analysis of rainfall rate estimation using radar measurements, the degree of uncertainty associated with the same measurement estimates was considered. The Z_h, Z_{dr}, and Φ_{dp} radar measurements were superimposed with random errors of 1 dB, 0.2 dB, and 3°, respectively. Under these conditions, R_{dp} shows a significant increase of NSE that becomes comparable to that for R_z, whereas R_{dr} presents the lowest NSE, on average less than 30% and 25% compared to the corresponding values of R_z and R_{dp}, respectively.

The study leads to two important results. First, the beam-broadening effect introduces a variability in range described in terms of an increasing NSE of about 20% on average due to a decorrelation between radar and ground rain rate related to the rain variability in the increasing size of the radar beam. Second, it is not possible to define the best radar rainfall algorithm over the entire domain of the rain's natural variability because of a partial overlapping of the 95% confidence intervals of the different algorithms. Even though merit factors of

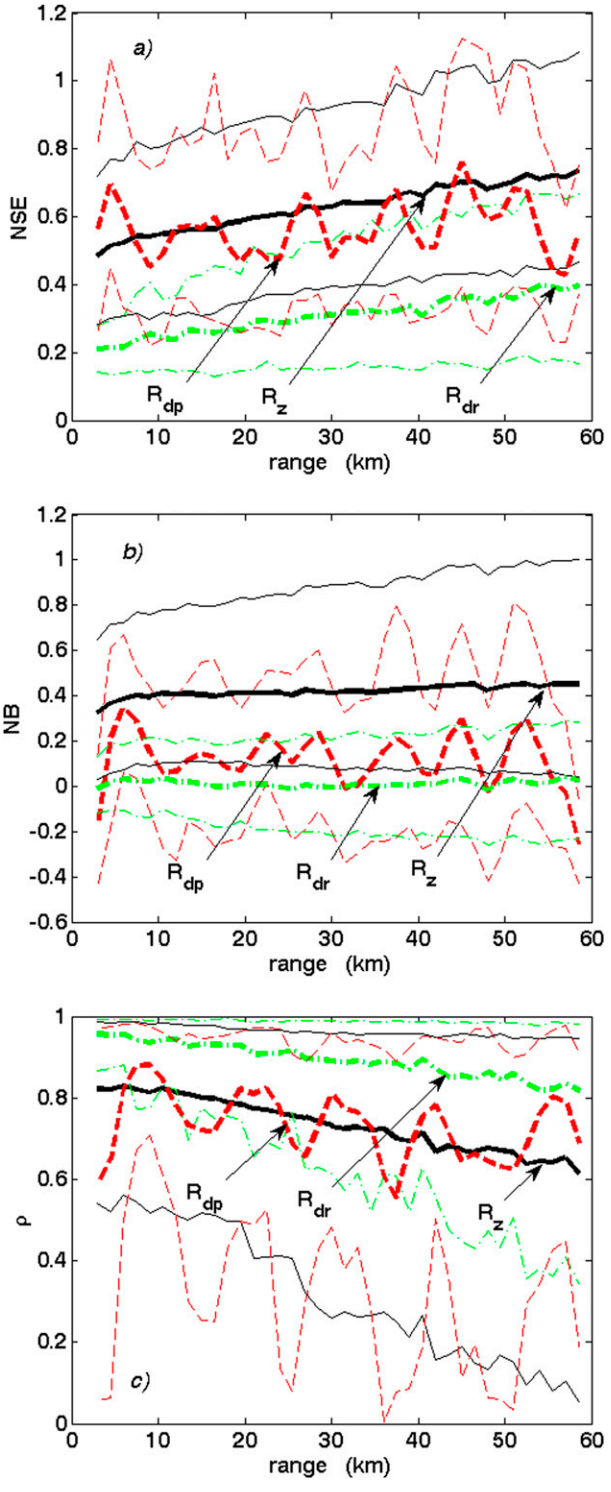

FIG. 9. As in Fig. 5, but for radar measurements that have been corrected for propagation effects and with noise added to radar measurements Z_h, Z_{dr}, and Φ_{dp} to simulate measurement errors.

hourly cumulative rainfall present a large improvement, the degree of overlapping of the 95% confidence intervals remains relatively constant.

Acknowledgments. This research was partially supported by the Italian Department of Civil Protection. Measurements from NASA MRR and 2DVD used in this study were collected as a contribution to the SOP1 of the HyMeX program. The authors also acknowledge the NASA Global Precipitation Measurement (GPM) mission ground validation program under Matthew Schwaller and Walter A. Petersen, GPM ground validation and science manager, respectively, for providing instruments and expertise. Finally, our thoughts go to the memory of Arthur Hou, former GPM project scientist, for his international vision throughout the GPM core-satellite prelaunch activities.

REFERENCES

Beard, K. V., and C. Chuang, 1987: A new model for the equilibrium shape of raindrops. *J. Atmos. Sci.,* **44,** 1509–1524, doi:10.1175/1520-0469(1987)044<1509:ANMFTE>2.0.CO;2.

Brandes, E. A., G. Zhang, and J. Vivekanandan, 2002: Experiments in rainfall estimation with a polarimetric radar in a subtropical environment. *J. Appl. Meteor.,* **41,** 674–685, doi:10.1175/1520-0450(2002)041<0674:EIREWA>2.0.CO;2.

Bringi, V. N., and V. Chandrasekar, 2001: *Polarimetric Doppler Weather Radar: Principles and Applications.* Cambridge University Press, 648 pp.

——, ——, N. Balakrishnan, and D. S. Zrnić, 1990: An examination of propagation effects in rainfall on polarimetric variables at microwave frequencies. *J. Atmos. Oceanic Technol.,* **7,** 829–840, doi:10.1175/1520-0426(1990)007<0829:AEOPEI>2.0.CO;2.

Chandrasekar, V., V. N. Bringi, N. Balakrishnan, and D. S. Zrnić, 1990: Error structure of multiparameter radar and surface measurements of rainfall. Part III: Specific differential phase. *J. Atmos. Oceanic Technol.,* **7,** 621–629, doi:10.1175/1520-0426(1990)007<0621:ESOMRA>2.0.CO;2.

Cifelli, R., V. Chandrasekar, S. Lim, P. C. Kennedy, Y. Wang, and S. A. Rutledge, 2011: A new dual-polarization radar rainfall algorithm: Application in Colorado precipitation events. *J. Atmos. Oceanic Technol.,* **28,** 352–364, doi:10.1175/2010JTECHA1488.1.

Doviak, R. J., and D. S. Zrnić, 1993: *Doppler Radar and Weather Observations.* 2nd ed. Academic Press, 562 pp.

Ferretti, R., and Coauthors, 2014: Overview of the first HyMeX Special Observation Period over Italy: Observations and model results. *Hydrol. Earth Syst. Sci.,* **18,** 1953–1977, doi:10.5194/hess-18-1953-2014.

Gorgucci, E., and G. Scarchilli, 1997: Intercomparison of multiparameter radar algorithms for estimating rainfall rate. Preprints, *28th Conf. on Radar Meteorology,* Austin, TX, Amer. Meteor. Soc., 55–56.

——, ——, V. Chandrasekar, and V. N. Bringi, 2001: Rainfall estimation from polarimetric radar measurements: Composite algorithms immune to variability in raindrop shape–size relation. *J. Atmos. Oceanic Technol.,* **18,** 1773–1786, doi:10.1175/1520-0426(2001)018<1773:REFPRM>2.0.CO;2.

Gosset, M., 2004: Effect of nonuniform beam filling on the propagation of radar signals at X-band frequencies. Part II: Examination of differential phase shift. *J. Atmos. Oceanic Technol.,* **21,** 358–367, doi:10.1175/1520-0426(2004)021<0358:EONBFO>2.0.CO;2.

Hubbert, J., and V. N. Bringi, 1995: An iterative filtering technique for the analysis of copolar differential phase and dual-frequency radar measurements. *J. Atmos. Oceanic Technol.,* **12,** 643–648, doi:10.1175/1520-0426(1995)012<0643:AIFTFT>2.0.CO;2.

Klugmann, D., and C. Richter, 1995: Correction of drop shape–induced errors on rain rates derived from radar-measured Doppler spectra at vertical incidence. *J. Atmos. Oceanic Technol.,* **12,** 657–661, doi:10.1175/1520-0426(1995)012<0657:CODSIE>2.0.CO;2.

Ryzhkov, A. V., 2007: The impact of beam broadening on the quality of radar polarimetric data. *J. Atmos. Oceanic Technol.,* **24,** 729–744, doi:10.1175/JTECH2003.1.

——, and D. Zrnić, 1998: Beamwidth effects on the differential phase measurements of rain. *J. Atmos. Oceanic Technol.,* **15,** 624–634, doi:10.1175/1520-0426(1998)015<0624:BEOTDP>2.0.CO;2.

——, S. E. Giangrande, and T. J. Schuur, 2003: Rainfall measurements with the polarimetric WSR-88D radar. National Severe Storms Laboratory Rep., 98 pp.

Sachidananda, M., and D. S. Zrnić, 1987: Rain rate estimates from differential polarization measurements. *J. Atmos. Oceanic Technol.,* **4,** 588–598, doi:10.1175/1520-0426(1987)004<0588:RREFDP>2.0.CO;2.

Scarchilli, G., E. Gorgucci, V. Chandrasekar, and T. A. Seliga, 1993: Rainfall estimation using polarimetric techniques at C-band frequencies. *J. Appl. Meteor.,* **32,** 1150–1160, doi:10.1175/1520-0450(1993)032<1150:REUPTA>2.0.CO;2.

Schönhuber, M., H. E. Urban, P. P. V. Poiares Baptista, W. L. Randeu, and W. Riedler, 1997: Weather radar versus 2D-video–disdrometer data. *Weather Radar Technology for Water Resources Management,* B. Bragg Jr. and O. Massambani, Eds., UNESCO Press, 159–171.

Tokay, A., and D. A. Short, 1996: Evidence from tropical raindrop spectra of the origin of rain from stratiform versus convective clouds. *J. Appl. Meteor.,* **35,** 355–371, doi:10.1175/1520-0450(1996)035<0355:EFTRSO>2.0.CO;2.

Tridon, F., J. Van Balen, and Y. Pointin, 2011: Aliasing in micro rain radar data due to strong vertical winds. *Geophys. Res. Lett.,* **38,** L02804, doi:10.1029/2010GL046018.

Vivekanandan, J., V. N. Bringi, and R. Raghavan, 1990: Multiparameter radar modeling and observations of melting ice. *J. Atmos. Sci.,* **47,** 549–563, doi:10.1175/1520-0469(1990)047<0549:MRMAOO>2.0.CO;2.

Waterman, P. C., 1965: Matrix formulation of electromagnetic scattering. *Proc. IEEE,* **53,** 805–812, doi:10.1109/PROC.1965.4058.

Zawadzki, I., 1984: Factors affecting the precision of radar measurements of rain. Preprints, *22nd Conf. Radar Meteorology,* Zurich, Switzerland, Amer. Meteor. Soc., 251–256.